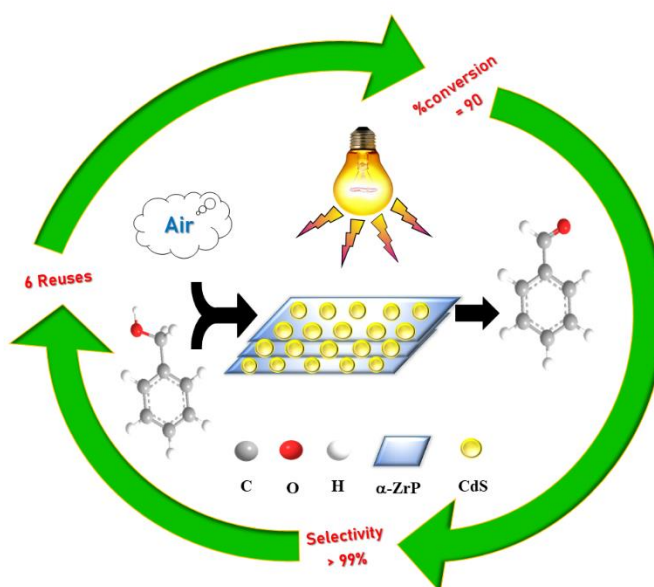**Chapter 4**

α-ZrP Supported CdS Quantum Dot Composite Material: An Efficient and Recyclable Photocatalyst for Selective Oxidation of Benzyl Alcohols

Abstract. α- zirconium phosphate nano-platelets are employed as a crystalline support for CdS quantum dots. A new composite material, where CdS quantum dots of average size 2-6 nm homogeneously dispersed over α- zirconium phosphate nano-platelets is prepared and characterized using analytical, spectroscopic, structural and microscopic studies. Chrono-amperometric and electrochemical impedance studies reveal the photocatalytic characteristics of the composite material. Further, the composite showed remarkable photocatalytic activity in oxidation of benzyl alcohols with high reusability.

4.1. Introduction

The discovery of photoelectrocatalytic splitting of water on TiO_2 electrodes by Fujishima and Honda triggered an outburst of activities for development of semiconductor photocatalyst [1]. Indeed, visible light-driven photocatalytic technology have now emerged one of the most promising greener alternatives for alleviating depletion of energy resources and degradation of natural environment and thereby sustain modern human society [2-3]. Nevertheless, design of efficient and reusable photocatalyst for selective organic transformations remain one of the most pressing challenges that needs to be addressed for bulk scale applications of photocatalytic technology in industry [4]. In this regard, semiconductor nanoparticles or quantum dots are the most widely explored class of compounds for conversion of solar energy to chemical energy under visible light irradiation. The unique size dependent electronic as well as optical properties of semiconductor nanoparticles or quantum dots offer immense possibilities to tune their photochemical characteristics and thereby optimize their photocatalytic behavior. Among the semiconductor based photocatalyst, CdS has drawn particular attention and so far, found application in several key transformations i.e., photocatalytic hydrogen production, reduction of CO_2 to hydrocarbon fuels and degradation of pollutants [5-10]. This can be primarily attributed to the relatively narrow bandgap of CdS (2.4 eV) for visible light response and moreover the conduction band edge potential is sufficiently negative for reduction of protons. Despite these remarkable photochemical characteristics, there exist several crucial issues that severely restrict utilization of pure CdS particles in photocatalysis and considerable efforts are currently being devoted to address these bottlenecks. The inherent vulnerability of CdS particles to undergo agglomeration resulting in significant reduction in surface area remains one of the major concerns for their application in photocatalysis [11]. Apart from that, the high recombination rate of photogenerated electron-hole pairs and the propensity to undergo photo-corrosion are also major deterrents in their industrial application [11]. The above limitations associated with bare CdS particles warranted development of composite materials where CdS particles are supported over polymers, noble metals, metal oxides, carbon-based materials etc. as promising photocatalyst [12-18]. Suitable modification of these composites offers significant potential to reduce electron-hole pair recombination as well as prevent agglomeration of CdS particles and thus result superior photocatalyst

activity. More recently, metal organic frameworks (MOFs) have emerged as promising solid support to fabricate semiconductor composites for photocatalytic applications [19-25]. This can be primarily attributed to not only the porous crystalline nature of MOFs but also to the endless possibilities to manipulate the physical/chemical characteristics of the voids. However, the poor thermal as well as hydrolytic stability associated with majority of carboxylate-based metal organic frameworks impede their application under harsh conditions and development of robust hybrid crystalline material remains a key challenge in this domain [26]. In this regard, α-zirconium phosphate (α-ZrP) has emerged as a promising support material for fabrication of photocatalytically active composite materials [27-31]. α-ZrP has a layered structure where zirconium atoms are bonded to monohydrogen phosphate groups on both side of the layer [32]. Easy exfoliations of microcrystalline α-ZrP into nanoplatelets along with the ability to exchange the protons by small monovalent or divalent cation have propelled its application in ion exchange, catalysis, photocatalysis, intercalation etc. [33-35]. Herein, a facile and easy procedure for fabrication of CdS quantum dot-based composite photocatalyst by treatment of Cd(II) exchanged α-ZrP with Na_2S is described. The composite material is characterized by analytical, spectroscopic, structural, microscopic, electrochemical and impedance measurements. The photocatalytic activity of the CdS quantum dot in oxidation of alcohols into corresponding aldehydes was investigated.

4.2. Materials and Methods

Starting materials were purchased from commercial sources and used without further purification. Solvents were purified by conventional techniques and distilled prior to use. Elemental analyses were performed on a Perkin Elmer Model PR 2400 series II elemental analyzer. Transmittance electron microscope and EDS were recorded on JEM-100 CX II. The powder X-ray diffraction patterns were recorded on a Bruker AXS D8 Focus X-ray diffractometer instrument using a nickel filtered CuKα (0.15418 nm) radiation source and scintillation counter detector. Infrared spectra were recorded on a Nicolet Impact I-410 FT-IR spectrometer as KBr diluted discs and a Perkin Elmer MIR-FIR FT-IR spectrometer. The UV- visible spectra were recorded in a Shimadzu UV 2450 spectrophotometer. Electrochemical impedance spectra (EIS) were recorded on LCR HIOKI IM3570 impedance meter. The Photoluminescence spectra were recorded on Horiba Fluoromax -4C Fluorescence Spectrophotometer.

4.3. Experimental Section

4.3.1. Synthesis of α-zirconium phosphate (α-ZrP)

A mixture of $ZrOCl_2.8H_2O$ (4g) and 6M H_3PO_4 (40 mL) was sealed into Teflon®-Lined pressure vessel and autoclave at 200 °C for 24 h respectively. After reaction, the mixture was centrifuged and washed with distilled water repeatedly for three times. The product was collected after centrifugation. The solid powder was then dried at 65 °C for 24 h. FT-IR (KBr, cm^{-1}): 3408(br), 2382(w), 1619(m, s), 1047(s), 597(w), 524(w).

4.3.2. Synthesis of CdS quantum dot supported over α-ZrP

50 mg α-ZrP and 20 mL distilled H_2O was stirred for 5 minutes. To the above solution $Cd(CH_3COO)_2.2H_2O$ (13.32 mg, 0.05 mmol) was added. The reaction mixture was stirred for 12 hours. Thereafter, the reaction mixture was centrifuged and washed several times with water to remove the excess Cd present in the solution. Thereafter, $Na_2S.xH_2O$ (3.90 mg, 0.05 mmol) was slowly added dropwise. The mixture was kept under stirring at room temperature for 12 hours and then the resulting mixture was centrifuged and washed several times by distilled water. FT-IR (KBr, cm^{-1}): 3513(br), 2374(w), 1633(m, s), 1047(s), 614(m), 534(m), 416(w).

4.3.3. Photocatalytic oxidation of benzyl alcohols

The photocatalytic oxidation of benzyl alcohol and its derivatives into corresponding aldehyde was performed in a 50 mL round bottom flask at room temperature. A 55-watt Xenon lamp was used as the visible light source to trigger the photocatalytic reaction. Acetonitrile was selected as the reaction medium for benzyl alcohol selective oxidation. 50 mg of catalyst was dispersed in the reaction mixture. The reaction mixture was kept under stirring in dark to reach the adsorption-desorption equilibrium for 30 minutes. The above reaction mixture was kept under stirring by irradiating the light for next 6 hours. The catalytic activity of benzyl alcohols was tested in absence of the catalyst and visible light source. It was confirmed that the oxidation reaction did not proceed in absence of both the catalyst and visible light source.

4.3.4. Catalyst reusability test

The catalyst was recyclable without much loss of activity. The used catalyst was washed several times with acetonitrile and water, dried at 60°C for 4h and further reused for

consecutively for 5 times. The catalyst showed 90% conversion rate upto 5th cycle for pure benzyl alcohol. The conversion rate decreased on the 6th cycle because of the decomposition of the catalyst as indicated by FT-IR spectra and powder X-ray diffraction pattern.

4.4. Results and Discussion

4.4.1. Synthesis and characterization of CdS QD@ α-ZrP

α-zirconium phosphate (α-ZrP) nanoplatelets decorated with uniformly dispersed CdS quantum dots can be easily accessed by a two-step procedure. Initially, exfoliated zirconium phosphate nanoplatelets were exposed to an aqueous solution containing Cd^{2+} ion. P-OH groups present on the surface of zirconium phosphate nanoplatelets coordinated to Cd^{2+} and thereby ensured a uniform dispersion of Cd^{2+} over the entire surface. Subsequent, treatment of the Cd^{2+} doped zirconium phosphate with Na_2S immediately produced a yellow solid which can be characterized as zirconium phosphate nanoplatelets decorated with CdS quantum dots, CdS@α-ZrP.

FT-IR spectra of the composite, CdS@α-ZrP compare well with the FT-IR spectra of pristine α-ZrP and thereby suggest the integrity of the zirconium phosphate support material in the composite. Intense and broad peaks centered at 1047 cm^{-1} (Figure 4.1) are characteristic of antisymmetric and symmetric P-O stretching vibrations respectively [36].
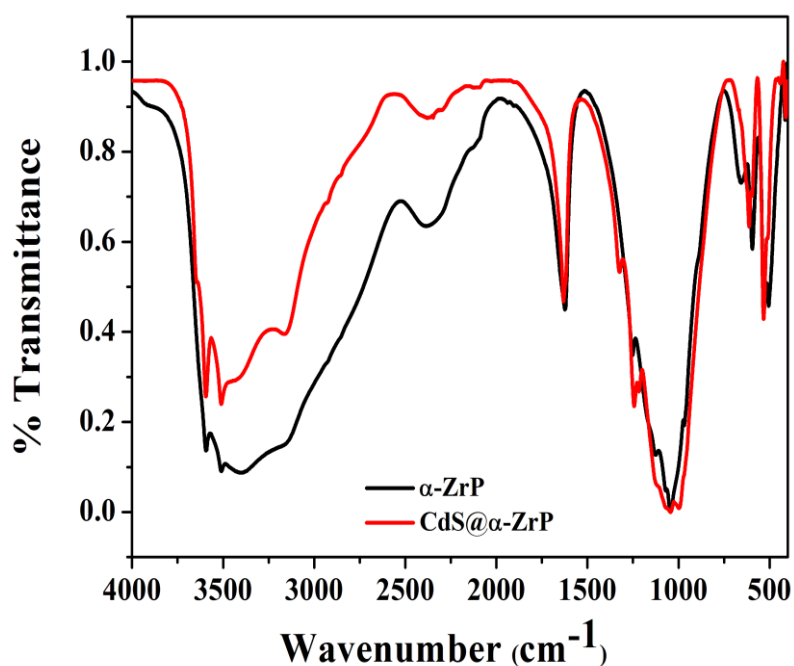

Figure 4.1. FT-IR spectrum of α-ZrP and CdS@α-ZrP

Weak and broad signal centered at 2382 cm^{-1} observed in the FT-IR spectra of CdS@α-ZrP can be assigned to P-O-H stretching vibration. An intense peak observed at 1619 cm^{-1} can be attributed to O-H deformation bending vibration of water molecules occluded within the interlayer space of CdS@α-ZrP [37].

Powder X-ray diffraction pattern of CdS@α-ZrP showed peaks corresponding to hexagonal wurtzite phase of CdS apart from the characteristic peaks associated to α-ZrP. Thus, integrity of the layered structure in α-ZrP is retained upon deposition of CdS particles over the surface of α-ZrP (Figure 4.2).
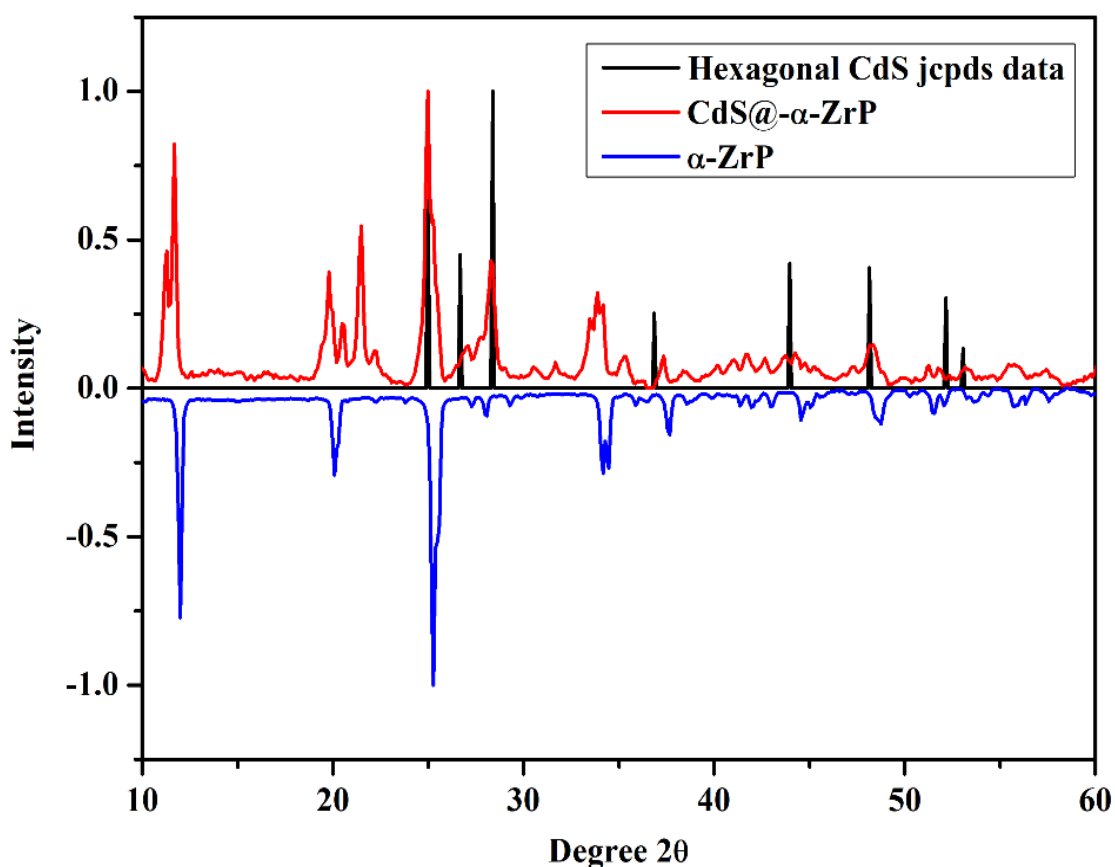

Figure 4.2. Powder XRD pattern of hexagonal CdS, α-ZrP and CdS@α-ZrP

Scanning electron microscopic analysis of pristine α-ZrP and CdS@α-ZrP revealed no appreciable modification in the particle size upon CdS loading and the layered plate shaped morphology α-ZrP crystallites are retained in the composite, CdS@α-ZrP (Figure 4.3 (a)). Transmission electron microscopic analysis of CdS@α-ZrP unambiguously established that CdS quantum dot of average size 2-6 nm are homogeneously dispersed over the α-ZrP nano-platelets without any apparent aggregation (Figure 4.3 (b-d)).
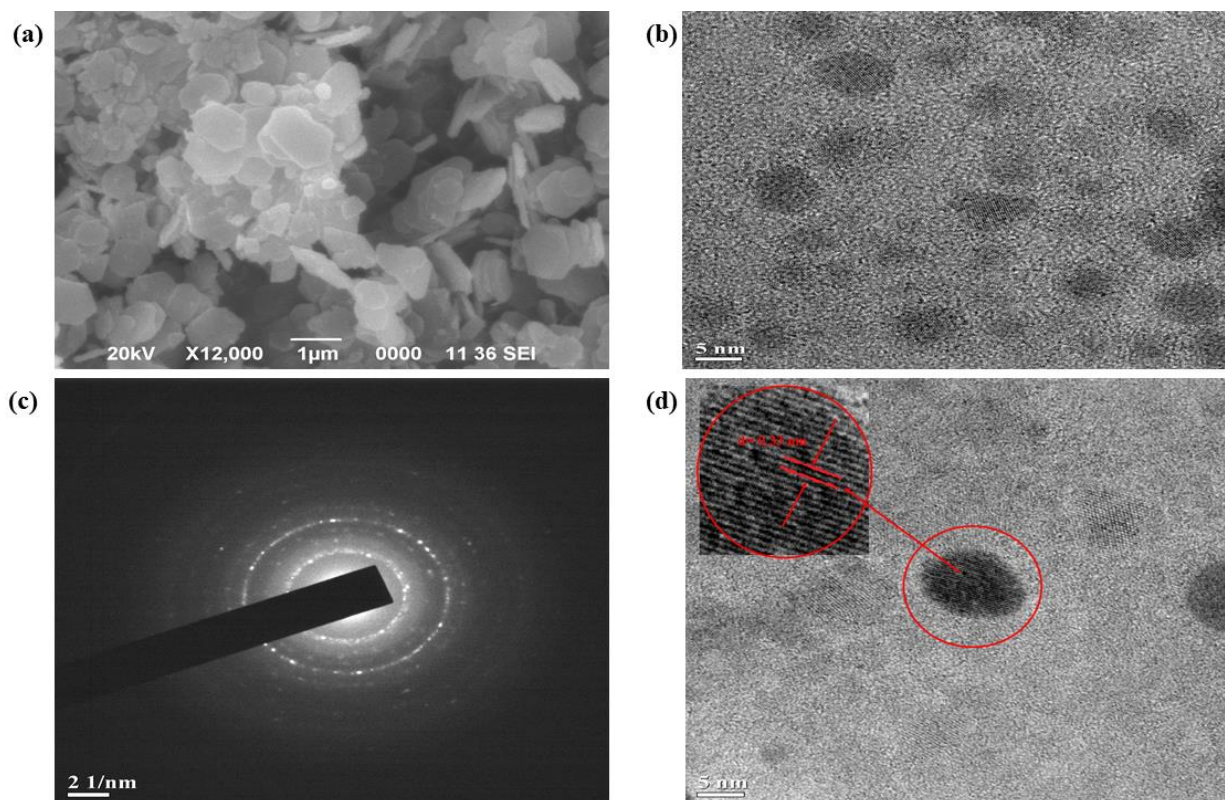
Figure 4.3. (a) SEM image of CdS@α-ZrP (b) TEM image of CdS@α-ZrP (c) Electron diffraction pattern of CdS@a-ZrP and (d) TEM image (lattice fringes) of CdS@a-ZrP quantam dots

Elemental mapping of CdS@α-ZrP shows the presence of zirconium, phosphorous, cadmium, sulphur and oxygen on the surface of the composite framework. Uniformly distribution of CdS nanoparticles over the surface of α-ZrP support (Figure 4.4 (i)) is established from the elemental mapping images. The loading of CdS obtained from energy dispersive X-ray spectroscopic mapping of CdS@α-ZrP was found to be 2.01 weight % (Figure 4.4 (ii)) and this value is in good agreement with the loading of CdS measured by atomic adsorption spectroscopy. Thus, in the composite, CdS@α-ZrP for every 20 units of $Zr(HPO_3)_2$ groups, one CdS unit is present. Uniform and low loading of semiconductor nanoparticles over the solid matrix is an important criterion for preventing catalyst agglomeration as well as to reduce photo-corrosion. We anticipate that the layered nature of α-ZrP with a limited interlayer space prevent agglomeration of CdS particles which facilitate formation of CdS quantum dots of 2-6 nm size with high photostability.
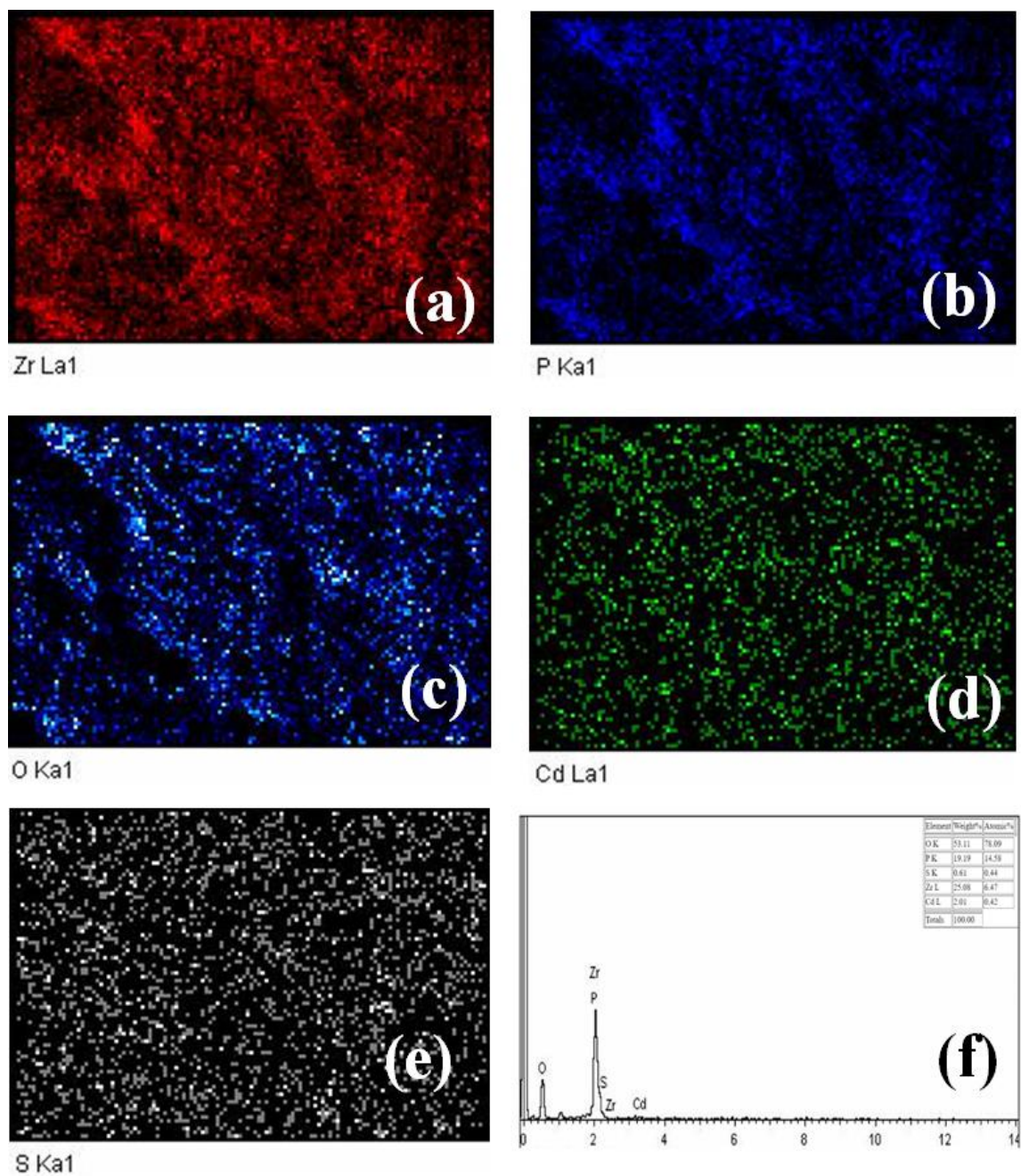
Figure 4.4. (i) Elemental mapping of (a) zirconium (b) phosphorus (c) oxygen (d) cadmium (e) sulphur in CdS@α-ZrP (ii) EDS of CdS@α-ZrP

Electronic properties of CdS quantum dots immobilized on α-ZrP was initially probed by using UV-visible diffuse reflectance spectroscopic studies. While the support, α-ZrP does not show any absorption between 200-800 nm range, the composite CdS@α-ZrP show adsorption edge characteristic of semiconducting material at 560 nm (Figure 4.5 (a)). The band gap energy of 2.35 eV estimated from the Tauc plot is close to that observed in case of bulk CdS (Figure 4.5 (b)).
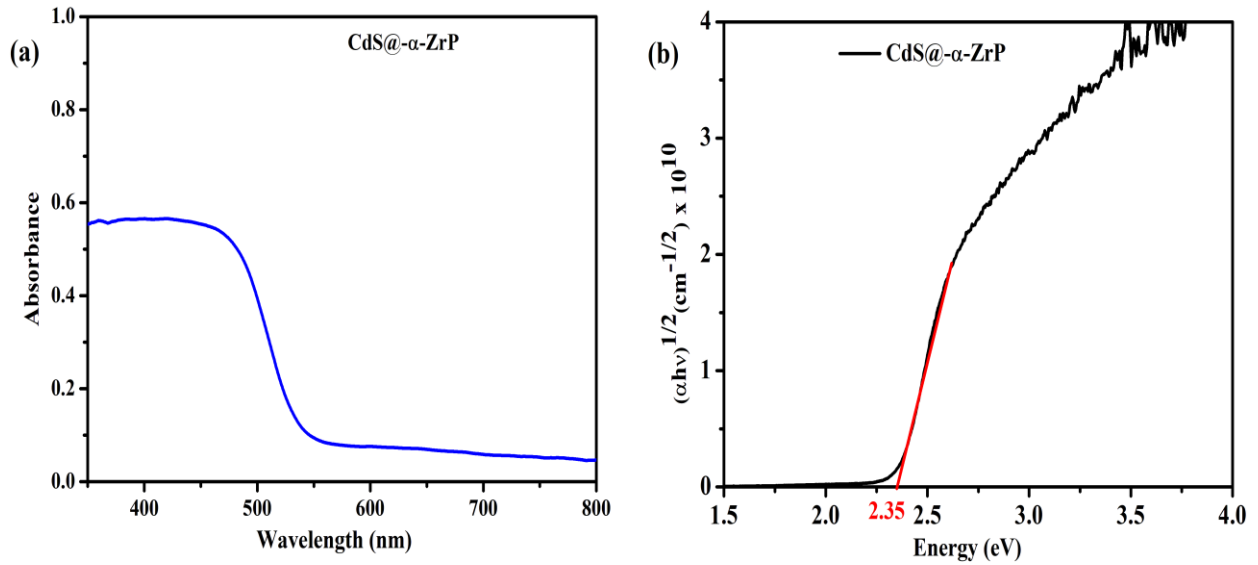
Figure 4.5. (a) UV-visible DRS spectrum of CdS@α-ZrP and (b) TAUC plot of CdS@α-ZrP

Photoluminescence studies of CdS@α-ZrP revealed that upon excitation at 450 nm, the CdS quantum dots dispersed over α-ZrP nanoplatelets show a broad emission centered at 519 nm (Figure 4.6). This emission band centered at 519 nm can be attributed to the emission of surface states due to the small size of the nanocrystals. Moreover, the band gap and the photoluminescence behaviour of CdS@α-ZrP did not show any appreciable variation over a long period and this clearly establish the stability of the nanoparticles against any agglomeration or photo-corrosion when immobilized over α-ZrP.
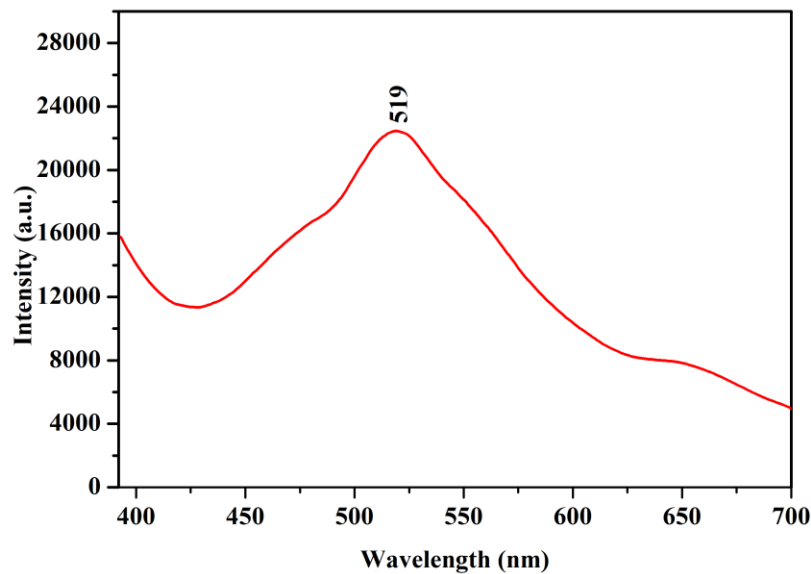

Figure 4.6. Photoluminescence spectrum of CdS@α-ZrP upon excitation at 450 nm

The thermogravimetric decomposition pattern of CdS@α-ZrP recorded under N_2 atmosphere at a heating rate of 10 °C/minute is depicted in Figure 4.7. The TGA pattern of CdS@α-ZrP show continuous weight loss till 250 °C and this can be attributed to the loss of occluded water molecules as well as loss of water due to condensation of P-OH groups. No mass loss is observed upon heating the sample beyond 250 °C and up to the highest temperature under measurement, 600 °C. Thus, thermogravimetric analysis reveal high thermal robustness of the composite, CdS@α-ZrP (Figure 4.7).
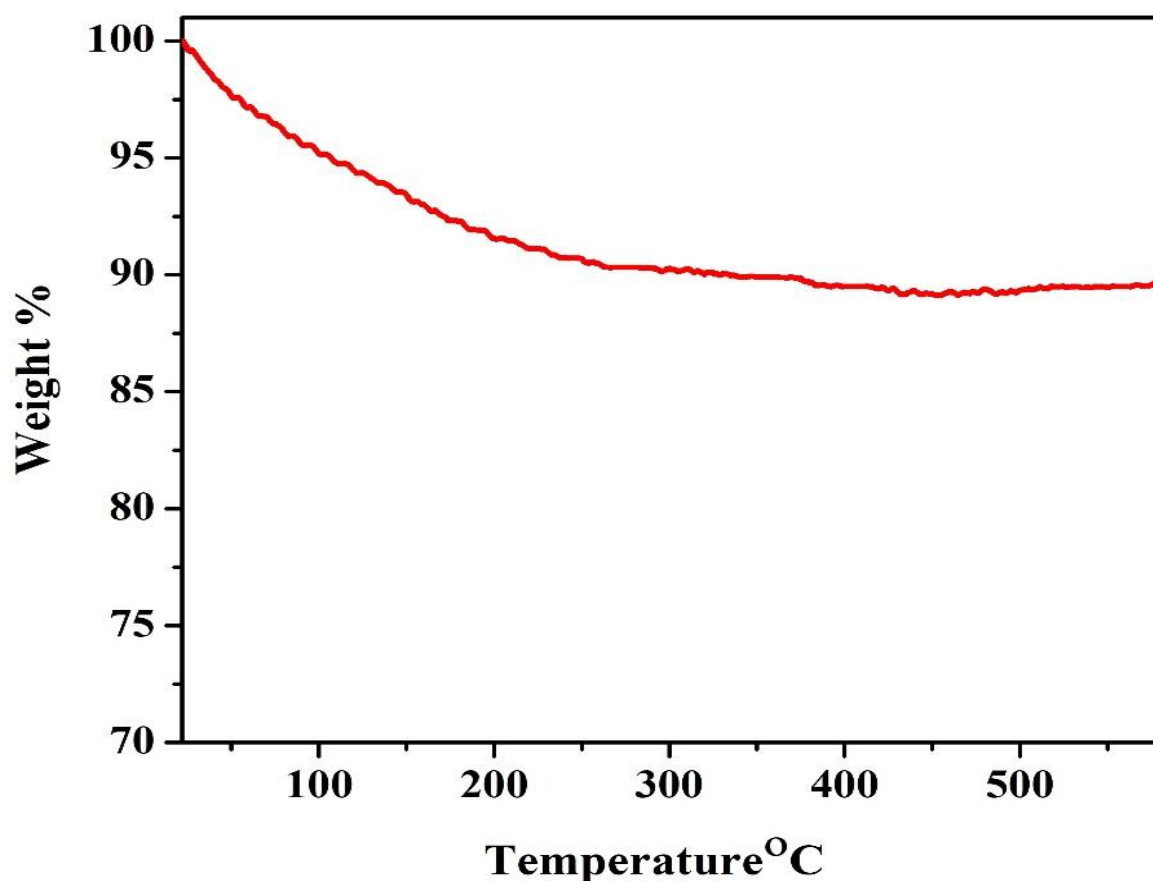

Figure 4.7. TGA pattern of CdS@α-ZrP under N_2 atmosphere

In order to assess the photocatalytic capacity of the composite CdS@α-ZrP, its photo-response was probed by chrono-amperometry under no applied voltage. Abrupt enhancement in photocurrent is observed upon exposure of the composite to light emitted by 55-watt Xenon lamp (Figure 4.8). Presence of photocurrent spikes in chronoamperometric study can be attributed incongruency in slow surface reaction dynamics and rapid generation of carriers. Further, a linear decrease in transient photo current during successive exposure cycle is observed due to accumulation of charge on the surface of CdS@α-ZrP [38-39].
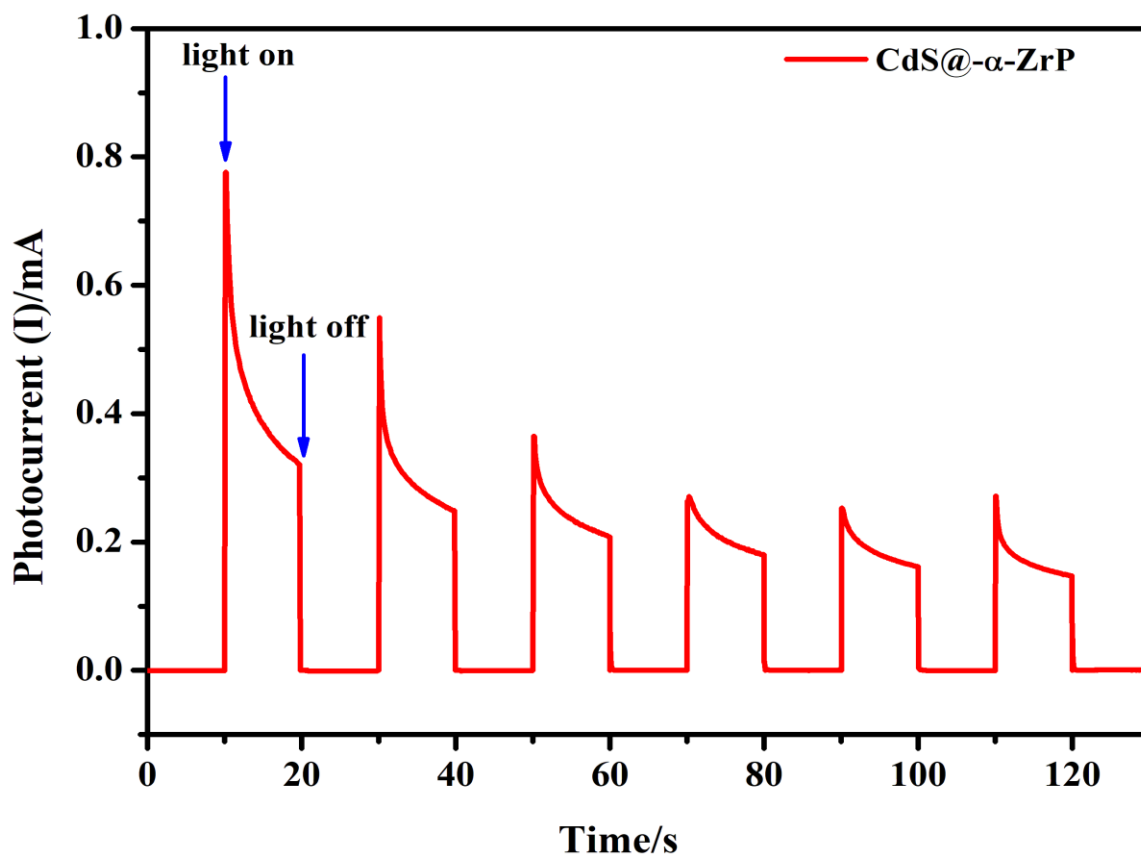
Figure 4.8. Transient photocurrents of CdS@α-ZrP

The mechanism of charge transfer within CdS@α-ZrP was probed by electrochemical impedance spectroscopic analysis of both pristine α-ZrP and CdS@α-ZrP within the temperature range 30-60 °C. No conceivable data was obtained in case of pristine α-ZrP as it has high resistance. However, Nyquist plot for CdS@α-ZrP reveal that upon introducing CdS QDs, the hole conductivity increases (Figure 4.9 (a)). This observation implies to an increment in equivalent resistance of the circuit that concur with the intrinsic behaviour of semiconductors (Figure 4.9 (b-h)). Further, it is observed that Nyquist plots for CdS@α-ZrP show an increase in radius of the semi-circular curves upon rise in temperature (Table 4.1).
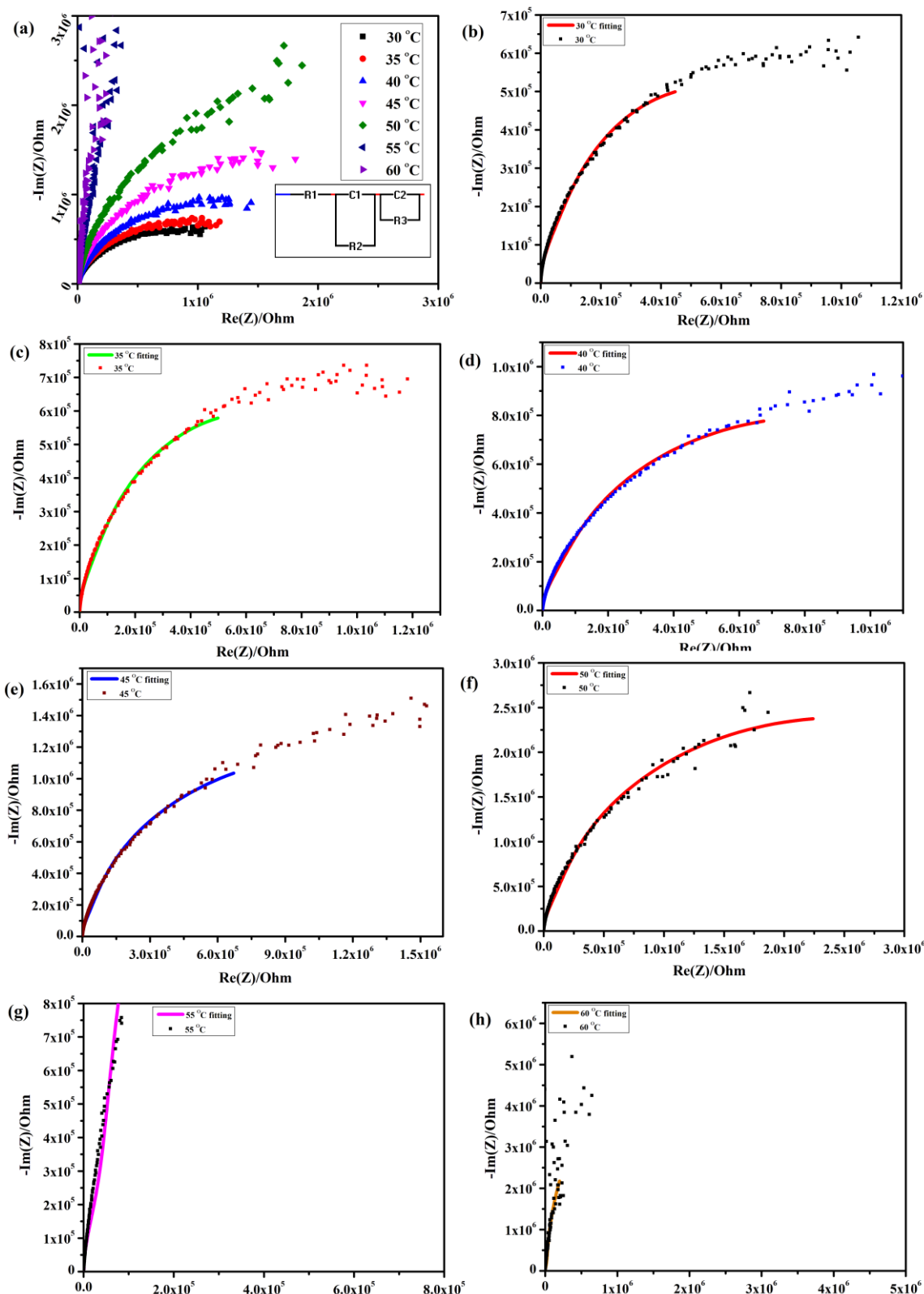
Figure 4.9. (a) Nyquist plot of CdS@α-ZrP (b) Nyquist plot fitting at 30 °C (c) Nyquist plot fitting at 35 °C (d) Nyquist plot fitting at 40 °C (e) Nyquist plot fitting at 45 °C (f) Nyquist plot fitting at 50 °C (g) Nyquist plot fitting at 55 °C (h) Nyquist plot fitting at 60 °C

Table 4.1. Circuit parameters calculated from Nyquist plot

Temperature (°C)	Bulk Resistance (R1) Ohm	Charge Transfer Resistance (R2) Ohm	Mass Transfer Resistance (R3) Ohm	Parallel Plate Capacitance Charge Transfer (C2) F	Parallel Plate Capacitance Mass Transfer (C3) F
30	891.1	160757	1.17×10^6	5.37×10^{-11}	6.38×10^{-11}
35	881.5	149445	1.36×10^6	5.83×10^{-11}	5.63×10^{-11}
40	874.9	145184	1.79×10^6	4.98×10^{-11}	6.47×10^{-11}
45	840.0	121005	2.71×10^6	4.21×10^{-11}	7.85×10^{-11}
50	824.9	121317	4.76×10^6	9.31×10^{-11}	3.73×10^{-11}
55	760.3	85009	4.03×10^7	3.30×10^{-11}	0.12×10^{-11}
60	665.7	46673	6.65×10^6	0.15×10^{-11}	2.97×10^{-11}

Arrhenius equation for the hole conductivities at different temperatures are plotted against T^{-1} and the activation energy (Ea) for hole transport was calculated accordingly was found to be 0.13 eV (Figure 4.10).
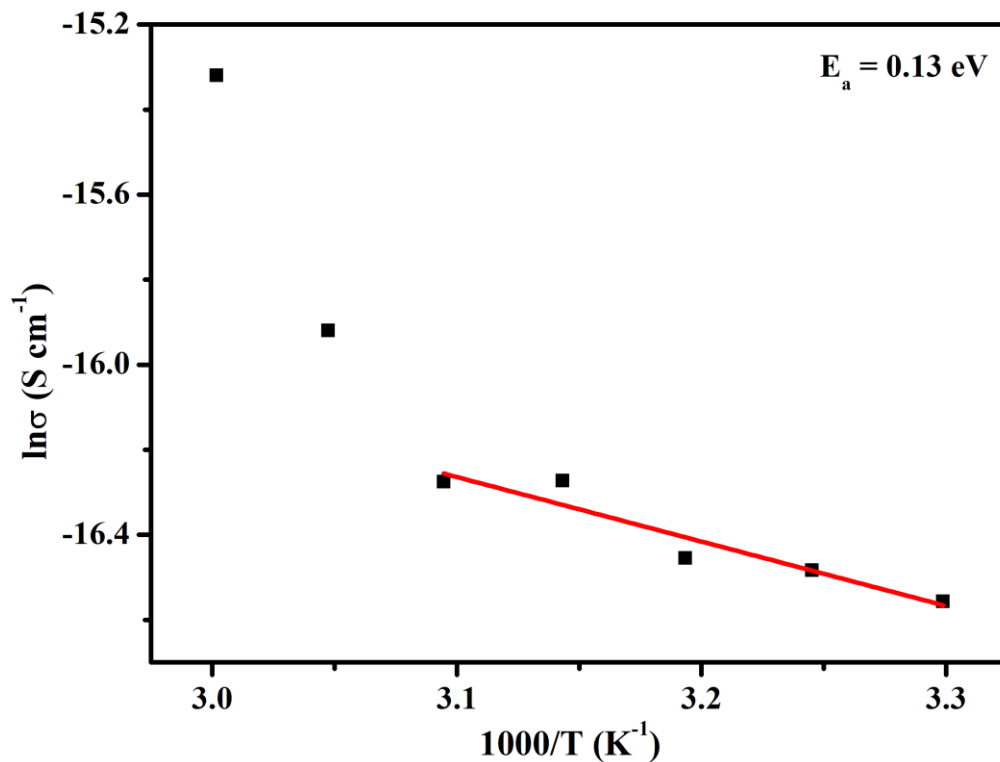
Figure 4.10. Arrhenius plot of hole conductivity vs T^{-1}

4.4.2. Photocatalytic activity of CdS QD@α-ZrP

The photocatalytic activity of the composite, CdS@α-ZrP was probed in oxidation of benzyl alcohol by using a 55-watt xenon lamp. The conversion of the precursor benzyl alcohol was determined by using high performance liquid chromatography (HPLC) and a HPCL calibration curve for benzyl alcohol is depicted in Figure 4.11(a). Up to 90% conversion of the precursor benzyl alcohol with 99% selectivity for aldehyde is achieved within a time span of 6 hours (Figure 4.11(b)).
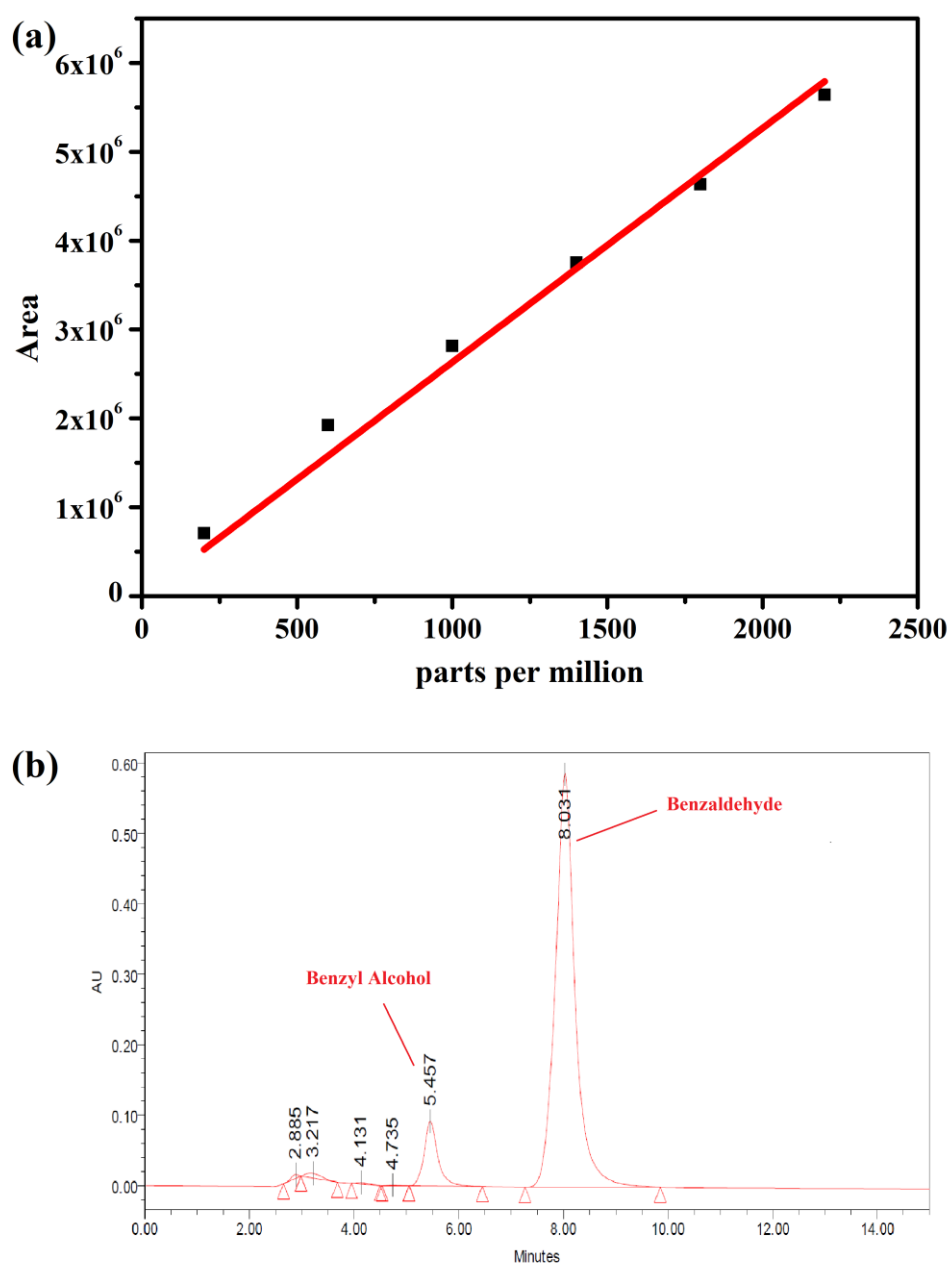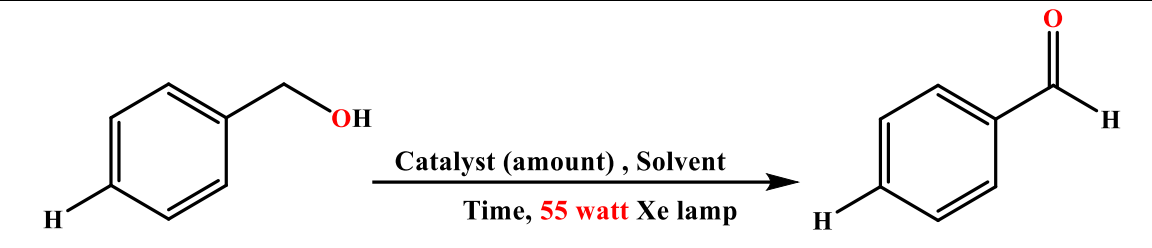

Figure 4.11. (a) HPLC calibration curve for benzyl alcohol (b) HPLC data of photo-catalytic oxidation of benzyl alcohol using CdS@α-ZrP as catalyst

Thereafter, the role of different reaction variables i.e., catalyst amount, time, amount of solvent etc. were studied in order to ascertain the optimum conditions for achieving high conversion rate along with high selectivity. The results of optimization reactions are listed in Table 4.2 and the best conversion was obtained within 6-hour reaction time when 50 mg catalyst was used in acetonitrile medium.

Table 4.2. Photocatalytic oxidation of benzyl alcohol under different reaction conditions
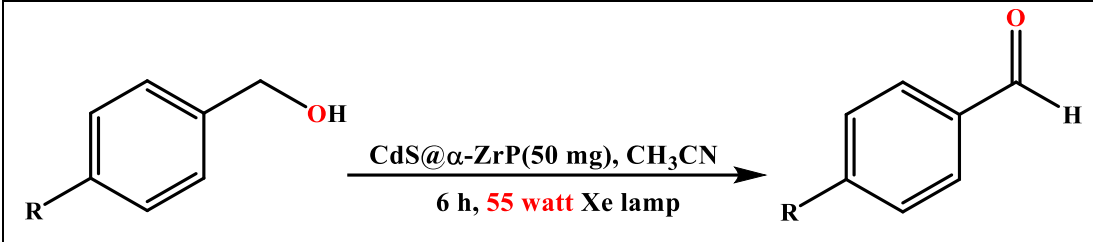
Solvent	Time (h)	Amount of Catalyst Used	% Conversion
CH$_3$CN	6	10 mg	50
CH$_3$CN	6	20 mg	55
CH$_3$CN	6	30 mg	70
CH$_3$CN	6	40 mg	75
CH$_3$CN	6	50 mg	90
CH$_3$CN	0.5	50 mg	15
CH$_3$CN	1	50 mg	20
CH$_3$CN	2	50 mg	35
CH$_3$CN	3	50 mg	50
CH$_3$CN	4	50 mg	60
CH$_3$CN	5	50 mg	80
CH$_3$CN	6	50 mg	90
CH$_3$CN	6	50 mg	90
CH$_3$OH	6	50 mg	60
Iso-Propanol	6	50 mg	45
Acetone	6	50 mg	20

Moreover, in order to explore the scope of the reaction and to understand the electronic effect of different substituents on the % conversion, above photocatalytic oxidation was investigated for six different benzyl alcohols. The results of these reactions are listed in

Table 4.3 and the results show no drastic decrease in the % conversions upon change in electronic nature of the substituents except when strongly electron withdrawing substituents are present.

Table 4.3. Optimization Table with different substrate

Substrate (R)	% Yield
$-OCH_3$	80
$-OH$	75
$-Br$	77
$-NO_2$	55
$-CH_3$	70
$-Cl$	65

To understand the primary reactive species involved in the selective oxidation of benzyl alcohol over CdS@α-ZrP under visible light irradiation the reaction was performed in the presence of different scavengers. Here, benzoquinone (BQ) was used to scavenge superoxide radical ($^{.}O_2^{-}$), ammonium oxalate (AO) for hole (h^+), *t*-BuOH for hydroxide radical ($^{.}OH$) and $AgNO_3$ for electron (e^-) respectively (Table 4.4). To determine the source of oxygen, the reaction was carried out under N_2 atmosphere for same reaction conditions as stated. But in N_2 atmosphere the reaction yielded the product in trace amounts and thus it can be stated that the oxidation process employs O_2 from the atmosphere.

Table 4.4. Percentage conversion and selectivity of aldehyde obtained in presence of different scavengers.

Scavenger	% Conversion	% Selectivity
Blank	90	99
t-BuOH	89	74
Ammonium Oxalate	72	98
p-Benzoquinone	18	91
$AgNO_3$	19	94

The maximum reduction in % conversion was observed in case of reactions carried out in presence of BQ and AgNO$_3$ (Figure 4.12 (a) and Figure 4.12 (b)). This confirms the participation of superoxide radical and electron in the photocatalytic oxidation process. A similar hindrance is observed with introduction of AO, showing that holes are also involved in the photochemical reaction (Figure 4.12 (c)). Moreover, near absence of any change in % conversion upon addition of *t*-BuOH indicate that ·OH radical is not a reactive species in the CdS@α-ZrP catalyzed photo-oxidation of benzyl alcohol (Figure 4.12 (d)). Hence from the above experiment it can be deduced that ·O$_2^-$, e$^-$ and h$^+$ plays an unequivocal role in the transformation of benzyl alcohol to benzaldehyde (Table 4.4, Figure 4.12).
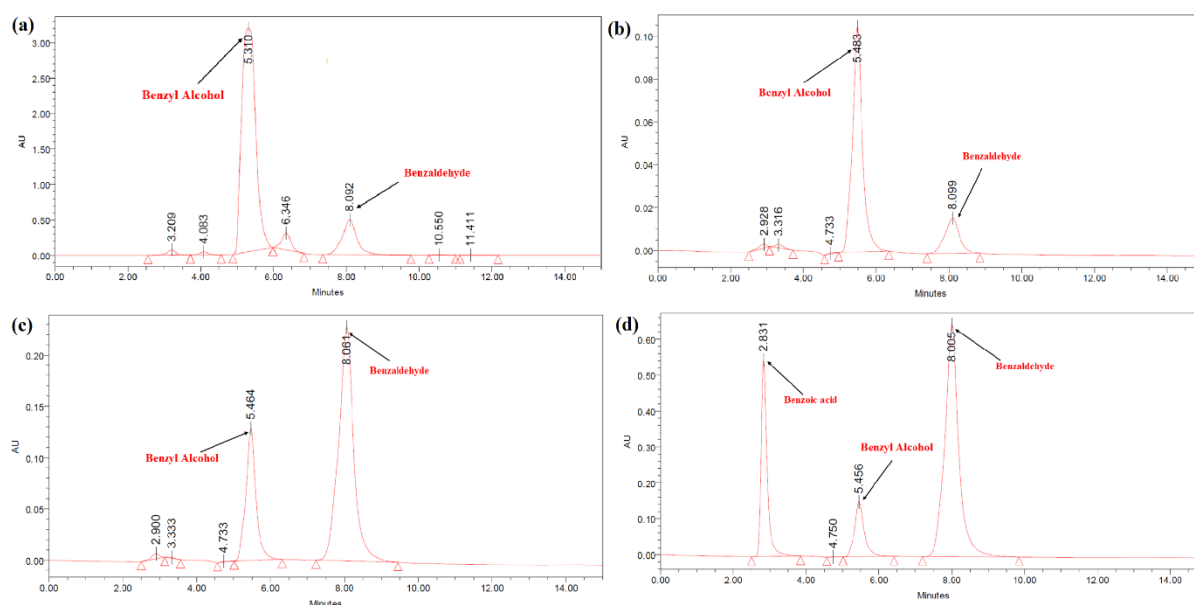

Figure 4.12. HPLC data for photo-catalytic oxidation of benzyl alcohol using CdS@α-ZrP as catalyst and using different radical scavenger (a) p-benzoquinone (b) AgNO$_3$ (c) ammonium oxalate (d) *t*-BuOH

To check the recyclability, the used catalyst was washed several times with acetonitrile and distilled water, dried at 60 °C for 4h and further reused for consecutively for five times. The catalyst showed 90% conversion rate up to 5th cycle while slight decrease in conversion rate was observed beyond 5th cycle. FT-IR spectra and powder X-ray diffraction pattern of used catalyst isolated after fifth cycle did not show any apparent sign of decomposition (Figure 4.13).
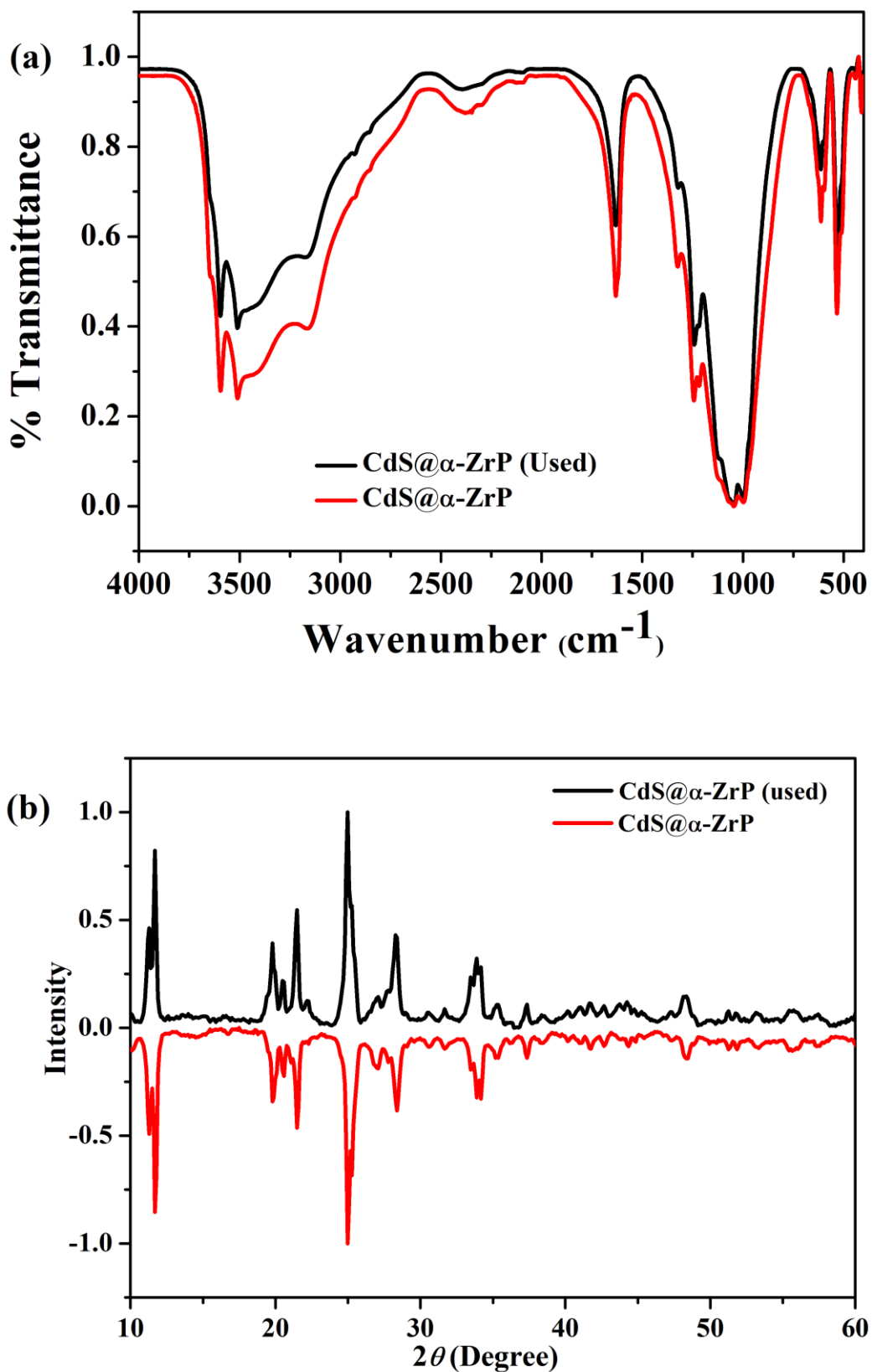
(a)

(b)

Figure 4.13. (a) FT-IR spectrum and (b) powder X-ray diffraction pattern of pristine CdS@α-ZrP and CdS@α-ZrP recovered after 5th photocatalytic cycle

Further, the catalytic efficacy and selectivity observed CdS@-α-ZrP catalyzed photo-oxidation of benzyl alcohol is comparable to those observed in case of metal oxide or metal sulphide supported CdS composites (Table 4.5) [38-44]. Nevertheless, the easy preparative technique, high photostability as well as thermal robustness of the present photocatalytic system demonstrate its potential as photocatalyst.

Table 4.5. Comparison of % conversion and % selectivity in CdS composite catalysed photo-oxidation of benzyl alcohol to bezaldehyde

Photocatalyst	Light Source	Time (h)	Conversion (%)	Selectivity (%)	Reusability	Reference
Ni(OH)$_2$ modified CdS-MoS$_2$	Visible Light	9	94	99	5	38
CdS/TiO$_2$	300W Xe Lamp	4	22	99	4	39
CdS	Visible light	8	44	90	4	40
CdS@MoS$_2$	Visible light	11	94	99	-	41
Ni-modified CdS	Visible light	20	96	96	-	42
GR-CdS	300W Xe Lamp	2	65	75	-	43
CdS@CeO$_2$	Visible Light	4	75.3	99	-	44
CdS@α-ZrP	55W Xe Lamp	6	90	99	6	This work

4.5. Conclusions

Thus, a composite material, CdS@α-ZrP wherein CdS quantum dots of size 2-6 nm are uniformly distributed over the surface of a layered solid support, α-ZrP is prepared and characterized using analytical, spectroscopic, structural and microscopic tools. The layered composite showed high thermal and photostability. Moreover, the composite showed good photocatalytic activity in aerobic oxidation of benzyl alcohol to benzaldehyde and can be recycled up to 6th cycle without any appreciable loss of efficiency. The present study demonstrate the unique ability of α-ZrP in immobilization of photocatalytically active species and thereby design photocatalyst with high photostability as well as recyclability.

4.6. References

[1]   Fujishima, A. and Honda, K. Electrochemical photolysis of water at a semiconductor electrode. *Nature*, 238(5358):37-38, 1972.

[2]   Kudo, A. and Miseki, Y. Heterogeneous photocatalyst materials for water splitting. *Chemical Society Reviews*, 38(1):253-278, 2009.

[3]   Qu, Y. and Duan, X. Progress, challenge and perspective of heterogeneous photocatalysts. *Chemical Society Reviews*, 42(7):2568-2580, 2013.

[4]   Serpone, N.A.V.E. and Emeline, A.V. Semiconductor Photocatalysis- Past, Present, and Future Outlook. *The journal of physical chemistry letters*, 3(5):673-677, 2012.

[5]   Zhang, K., Kim, W., Ma, M., Shi, X., and Park, J.H. Tuning the charge transfer route by p–n junction catalysts embedded with CdS nanorods for simultaneous efficient hydrogen and oxygen evolution. *Journal of Materials Chemistry A*, 3(9):4803-4810, 2015.

[6]   Jin, J., Yu, J., Liu, G., and Wong, P.K. Single crystal CdS nanowires with high visible-light photocatalytic H_2-production performance. *Journal of Materials Chemistry A*, 1(36):10927-10934, 2013.

[7]   Wu, A., Tian, C., Jiao, Y., Yan, Q., Yang, G., and Fu, H. Sequential two-step hydrothermal growth of MoS_2/CdS core-shell heterojunctions for efficient visible light-driven photocatalytic H_2 evolution. *Applied Catalysis B: Environmental*, 203:955-963, 2017.

[8]   Zhong, Y., Zhao, G., Ma, F., Wu, Y., and Hao, X. Utilizing photocorrosion-recrystallization to prepare a highly stable and efficient CdS/WS2 nanocomposite photocatalyst for hydrogen evolution. *Applied Catalysis B: Environmental*, 199:466-472, 2016.

[9]   Tian, Q., Wu, W., Liu, J., Wu, Z., Yao, W., Ding, J., and Jiang, C. Dimensional heterostructures of 1D CdS/2D ZnIn 2 S 4 composited with 2D graphene: designed synthesis and superior photocatalytic performance. *Dalton Transactions*, 46(9):2770-2777, 2017.

[10]   Lin, Y.F. and Hsu, Y.J. Interfacial charge carrier dynamics of type-II semiconductor nanoheterostructures. *Applied Catalysis B: Environmental*, 130:93-98, 2013.

[11]   Cheng, L., Xiang, Q., Liao, Y., and Zhang, H. CdS-based photocatalysts. *Energy & Environmental Science*, 11(6):1362-1391, 2018.

[12]   Liang, Q., Jiang, G., Zhao, Z., Li, Z., and MacLachlan, M.J. CdS-decorated triptycene-based polymer: durable photocatalysts for hydrogen production under visible-light irradiation. *Catalysis Science & Technology*, 5(6):3368-3374, 2015.

[13]   Ma, F., Zhao, G., Li, C., Wang, T., Wu, Y., Lv, J., Zhong, Y., and Hao, X. Fabrication of CdS/BNNSs nanocomposites with broadband solar absorption for efficient photocatalytic hydrogen evolution. *CrystEngComm*, 18(4):631-637, 2016.

[14]   Bera, R., Kundu, S., and Patra, A. 2D hybrid nanostructure of reduced graphene oxide–CdS nanosheet for enhanced photocatalysis. *ACS Applied Materials & Interfaces*, 7(24):13251-13259, 2015.

[15]   Xie, Y., Ali, G., Yoo, S.H., and Cho, S.O. Sonication-assisted synthesis of CdS quantum-dot-sensitized TiO2 nanotube arrays with enhanced photoelectrochemical and photocatalytic activity. *ACS applied materials & interfaces*, 2(10):2910-2914, 2010.

[16]   Wang, C., Wang, L., Jin, J., Liu, J., Li, Y., Wu, M., Chen, L., Wang, B., Yang, X., and Su, B.L. Probing effective photocorrosion inhibition and highly improved photocatalytic hydrogen production on monodisperse PANI@ CdS core-shell nanospheres. *Applied Catalysis B: Environmental*, 188:351-359, 2016.

[17]   Jiang, D., Sun, Z., Jia, H., Lu, D., and Du, P. A cocatalyst-free CdS nanorod/ZnS nanoparticle composite for high-performance visible-light-driven hydrogen production from water. *Journal of Materials Chemistry A*, 4(2):675-683, 2016.

[18]   Wu, A., Tian, C., Jiao, Y., Yan, Q., Yang, G., and Fu, H. Sequential two-step hydrothermal growth of MoS2/CdS core-shell heterojunctions for efficient visible light-driven photocatalytic H2 evolution. *Applied Catalysis B: Environmental*, 203:955-963, 2017.

[19]   Jin, S., Son, H.J., Farha, O.K., Wiederrecht, G.P., and Hupp, J.T. Energy transfer from quantum dots to metal–organic frameworks for enhanced light harvesting. *Journal of the American Chemical Society*, 135(3):955-958, 2013.

[20]   Esken, D., Turner, S., Wiktor, C., Kalidindi, S.B., Van Tendeloo, G., and Fischer, R.A. GaN@ ZIF-8: Selective formation of gallium nitride quantum dots inside a zinc methylimidazolate framework. *Journal of the American Chemical Society*, 133(41):16370-16373, 2011.

[21]   Ke, F., Wang, L., and Zhu, J. Facile fabrication of CdS-metal-organic framework nanocomposites with enhanced visible-light photocatalytic activity for organic transformation. *Nano Research*, 8(6):1834-1846, 2015.

[22]   Liu, Q., Low, Z.X., Li, L., Razmjou, A., Wang, K., Yao, J., and Wang, H. ZIF-8/Zn 2 GeO 4 nanorods with an enhanced CO 2 adsorption property in an aqueous medium for photocatalytic synthesis of liquid fuel. *Journal of Materials Chemistry A*, 1(38):11563-11569, 2013.

[23]   Li, R., Hu, J., Deng, M., Wang, H., Wang, X., Hu, Y., Jiang, H.L., Jiang, J., Zhang, Q., Xie, Y., and Xiong, Y. Integration of an inorganic semiconductor with a metal–organic framework: a platform for enhanced gaseous photocatalytic reactions. *Advanced Materials*, 26(28):4783-4788, 2014.

[24]   Crake, A., Christoforidis, K.C., Kafizas, A., Zafeiratos, S., and Petit, C. CO2 capture and photocatalytic reduction using bifunctional TiO2/MOF nanocomposites under UV–vis irradiation. *Applied Catalysis B: Environmental*, 210:131-140, 2017.

[25]   Su, Y., Zhang, Z., Liu, H., and Wang, Y. Cd0. 2Zn0. 8S@ UiO-66-NH2 nanocomposites as efficient and stable visible-light-driven photocatalyst for H2 evolution and CO2 reduction. *Applied Catalysis B: Environmental*, 200:448-457, 2017.

[26]   Ding, M., Cai, X., and Jiang, H.L. Improving MOF stability: approaches and applications. *Chemical Science*, 10(44):10209-10230, 2019.

[27]   Pica, M., Donnadio, A., and Casciola, M. From microcrystalline to nanosized α-zirconium phosphate: Synthetic approaches and applications of an old material with a bright future. *Coordination Chemistry Reviews*, 374:218-235, 2018.

[28]   Xiao, H., and Liu, S. Zirconium phosphate (ZrP)-based functional materials: Synthesis, properties and applications. *Materials & Design*, 155:19-35, 2018.

[29]   Pica, M., Nocchetti, M., Ridolfi, B., Donnadio, A., Costantino, F., Gentili, P.L., and Casciola, M. Nanosized zirconium phosphate/AgCl composite

materials: a new synergy for efficient photocatalytic degradation of organic dye pollutants. *Journal of Materials Chemistry A*, 3(10):5525-5534, 2015.

[30] Martí, A.A. and Colón, J.L. Photophysical characterization of the interactions among tris (2, 2′-bipyridyl) ruthenium (II) complexes ion-exchanged within zirconium phosphate. *Inorganic chemistry*, 49(16):7298-7303, 2010.

[31] Xu, Y., Zhou, F., Chen, M., Hu, H., Lin, L., Wu, J., and Zhang, M. Facile assembly of 2D α-zirconium phosphate supported silver nanoparticles: superior and recyclable catalysis. *New Journal of Chemistry*, 44(23):9793-9801, 2020.

[32] Clearfield, A. and Smith, G.D. Crystallography and structure of. alpha.-zirconium bis (monohydrogen orthophosphate) monohydrate. *Inorganic Chemistry*, 8(3):431-436, 1969.

[33] Clearfield, A. Metal phosphonate chemistry. *Progress in inorganic chemistry*, 47:371-510, 1998.

[34] Cao, G., Hong, H.G., and Mallouk, T.E. Layered metal phosphates and phosphonates: from crystals to monolayers. *Accounts of chemical research*, 25(9):420-427, 1992.

[35] Mallouk, T.E. and Julia, A.G. Molecular recognition in lamellar solids and thin films. 1997.

[36] Yang, H.C., Aoki, K., Hong, H.G., Sackett, D.D., Arendt, M.F., Yau, S.L., Bell, C.M., and Mallouk, T.E. Growth and characterization of metal (II) alkanebisphosphonate multilayer thin films on gold surfaces. *Journal of the American Chemical Society*, 115(25):11855-11862, 1993.

[37] Pica, M., Donnadio, A., Capitani, D., Vivani, R., Troni, E., and Casciola, M. Advances in the chemistry of nanosized zirconium phosphates: A new mild and quick route to the synthesis of nanocrystals. *Inorganic chemistry*, 50(22):11623-11630, 2011.

[38] Cui, C., Zhao, X., Su, X., Gao, W., Zhan, J., Zhang, X., Li, G., Zhang, X.L., Sang, Y., and Liu, H. Selective oxidation of benzyl alcohol using a Ni (OH) 2-modified CdS-MoS2 composite photocatalyst under ambient conditions. *Journal of Environmental Chemical Engineering*, 9(6):106416, 2021.

[39] Qin, N., Liu, Y., Wu, W., Shen, L., Chen, X., Li, Z., and Wu, L. One-dimensional CdS/TiO2 nanofiber composites as efficient visible-light-driven photocatalysts for selective organic transformation: synthesis, characterization, and performance. *Langmuir*, 31(3):1203-1209, 2015.

[40]   Liu, Y., Zhang, P., Tian, B., and Zhang, J. Core–shell structural CdS@ SnO2 nanorods with excellent visible-light photocatalytic activity for the selective oxidation of benzyl alcohol to benzaldehyde. *ACS applied materials & interfaces*, 7(25):13849-13858, 2015.

[41]   Li, P., Zhao, H., Yan, X., Yang, X., Li, J., Gao, S., and Cao, R. Visible-light-driven photocatalytic hydrogen production coupled with selective oxidation of benzyl alcohol over CdS@ MoS2 heterostructures. *Science China Materials*, 63(11):2239-2250, 2020.

[42]   Chai, Z., Zeng, T.T., Li, Q., Lu, L.Q., Xiao, W.J., and Xu, D. Efficient visible light-driven splitting of alcohols into hydrogen and corresponding carbonyl compounds over a Ni-modified CdS photocatalyst. *Journal of the American Chemical Society*, 138(32):10128-10131, 2016.

[43]   Ren, Z., Zhang, J., Xiao, F.X., and Xiao, G. Revisiting the construction of graphene–CdS nanocomposites as efficient visible-light-driven photocatalysts for selective organic transformation. *Journal of Materials Chemistry A*, 2(15):5330-5339, 2014.

[44]   Zhang, P., Liu, Y., Tian, B., Luo, Y., and Zhang, J. Synthesis of core-shell structured CdS@ CeO2 and CdS@ TiO2 composites and comparison of their photocatalytic activities for the selective oxidation of benzyl alcohol to benzaldehyde. *Catalysis Today*, 281:181-188, 2017.